DGTD Analysis of Electromagnetic Scattering From Penetrable Conductive Objects With IBC

Ping Li, *Member, IEEE*, Yifei Shi, *Member, IEEE*, Li Jun Jiang, *Senior Member, IEEE*, and Hakan Bağcı, *Senior Member, IEEE*

***Abstract*—To avoid straightforward volumetric discretization, a discontinuous Galerkin time-domain (DGTD) method integrated with the impedance boundary condition (IBC) is presented in this paper to analyze the scattering from objects with finite conductivity. Two situations are considered. 1) The skin depth is smaller than the thickness of the conductive volume. 2) The skin depth is larger than the thickness of a thin conductive sheet. For the first situation, a surface impedance boundary condition (SIBC) is employed, wherein the surface impedance usually exhibits a complex relation with the frequency. To incorporate the SIBC into DGTD, the surface impedance is first approximated by rational functions in the Laplace domain using the fast relaxation vector-fitting (FRVF) technique. Via inverse Laplace transform, the time-domain DGTD matrix equations can be obtained conveniently in integral form with respect to time t. For the second situation, a transmission IBC (TIBC) is used to include the transparent effects of the fields. In the TIBC, the tangential magnetic field jump is related with the tangential electric field via the surface conductivity. In this work, a specifically designed DGTD algorithm with TIBC is developed to model the graphene up to the terahertz (THz) band. In order to incorporate the TIBC into DGTD without involving the time-domain convolution, an auxiliary surface polarization current governed by a first-order differential equation is introduced over the graphene. For open-region scattering problems, the DGTD algorithm is further hybridized with the time-domain boundary integral (TDBI) method to rigorously truncate the computational domain. To demonstrate the accuracy and applicability of the proposed algorithm, several representative examples are provided.**

***Index Terms*—Auxiliary differential equation (ADE), discontinuous Galerkin time-domain (DGTD) method, finite integral technique (FIT), graphene, surface/transmission impedance boundary condition (SIBC/TIBC), time-domain boundary integral (TDBI) algorithm, vector-fitting.**

I. Introduction

To ANALYZE the electromagnetic scattering from penetrable structures, the standard numerical methods such as finite difference time-domain (FDTD) method [1], finite element method (FEM) [2], and discontinuous Galerkin time-domain (DGTD) method [4] require the discretization of the interior regions of the scatterers. To guarantee the accuracy, particularly fine spatial mesh elements are unavoidable, thus resulting in a larger number of unknowns and stringent Courant–Friedrichs–Lewy (CFL) condition for the time-domain solvers with explicit marching scheme. Usually, the average mesh size l_e for a conducting object with skin depth δ is around $\alpha \cdot \delta/20$, where α is a parameter dependent on the order of basis function, the solver used, etc.

Based on the fact that the electromagnetic waves are highly attenuated in good conducting medium, an impedance boundary condition (IBC) [2], [5] can be applied to replace the conducting object. Thus, volumetric discretization is no longer required. For a conductive structure with skin depth smaller than its thickness, the tangential components of the electric and magnetic fields over the surface of object are correlated with each other by a frequency dependent surface impedance Z_s [6], [9], which can be formulated as a surface impedance boundary condition (SIBC) [10]. The SIBC was first proposed by Leontovich [11] and later a rigorous model was developed by Senior [12]. Over the past years, the SIBC has already been integrated into FDTD [6]–[8], FEM–[14], and integral equation (IE)-based algorithms [15], [16] to solve the scattering, reflection, and transmission from imperfectly conductive objects.

For conductors with thickness on the order or far smaller than the skin depth, the effects of the electromagnetic fields transmitted to the other side of the conductor must be taken into account. In this case, a transmission IBC (TIBC) is required by relating the difference between the tangential magnetic field over the two sides of the thin conductor to the tangential electric field via an impedance matrix [17]. In [18], the TIBC is successfully integrated into an FDTD approach to study the shielding effectiveness of a thin conductive sheet, where the skin depth is on the order of the thickness of conductor. As an ideal candidate of the thin conductive sheet, the atom-thick graphene has been thoroughly investigated via the state-of-the-art analytical and numerical methods. In [19], a Dyadic Green's function (DGF) subjected to the TIBC is derived for an infinite long free-standing graphene ribbon. Based on this DGF, the radiation from a current source in the presence of graphene ribbons can be exactly calculated. In [20]–[22], the TIBC is incorporated into FDTD and IE solvers to analyze the interaction between the electromagnetic wave and the graphene, where the transmission, reflection, and absorption of electromagnetic waves, the surface plasmon resonance, and the far-field scattering are characterized, etc.

Manuscript received April 20, 2015; revised July 01, 2015; accepted July 25, 2015. Date of publication October 16, 2015; date of current version November 25, 2015.

P. Li, Y. Shi, and H. Bağcı are with the Division of Computer, Electrical, and Mathematical Sciences and Engineering, the Center for Uncertainty Quantification in Computational Science and Engineering, King Abdullah University of Science and Technology (KAUST), Thuwal 23955-6900, Saudi Arabia (e-mail: ping.li@kaust.edu.sa; yifei.shi@kaust.edu.sa; hakan.bagci@kaust.edu.sa).

L. J. Jiang is with the Department of Electrical and Electronic Engineering, University of Hong Kong, 00852 Hong Kong (e-mail: jianglj@hku.hk).

Color versions of one or more of the figures in this paper are available online at http://ieeexplore.ieee.org.

Digital Object Identifier 10.1109/TAP.2015.2491969

In this work, the SIBC-enhanced DGTD scheme is developed to study the electromagnetic scattering from conductive volumes. Simultaneously, a DGTD algorithm combined with TIBC is specifically designed to analyze the electromagnetic interaction with graphene from microwave to terahertz (THz) frequencies. As the combination of finite volume method (FVM) [23] and FEM [2], DGTD [4], [24]–[27] is capable of achieving high-order accuracy and involves only local operations. The resultant mass matrices are block-diagonal, and the finalized matrix system can be solved efficiently with explicit marching scheme. Since all boundary conditions are implemented into DGTD by reformulating the numerical flux based on the *Rankine–Hugoniot jump relations* [23], the analytical expression of numerical flux in the time-domain must be available in order to facilitate the DGTD analysis. However, the surface impedance or surface conductivity in the IBCs is usually a very complex function of the frequency, thus the time-domain counterpart of the numerical flux is not available via analytical inverse Fourier transform. To overcome this problem, the surface impedance Z_s involved in SIBC is approximated by rational functions in the Laplace domain using fast-relaxation vector-fitting (FRVF) method [28], [29]. Via inverse Laplace transform, then, the time-domain counterpart can be readily obtained according to the fact that division of the function by the state variable ($s = j\omega$) in the Laplace domain is an integral operation in the time-domain [27]. Resorting to the finite integral technique (FIT), the matrix equations in integral form are discretized into a fully discrete matrix system. On the other hand, the surface conductivity of the graphene with only intraband contribution is in a Drude-model form (below or in the THz band, the intraband term usually overwhelms the interband term); thus, an auxiliary differential equation (ADE) method [30] is exploited to incorporate the TIBC for the graphene into DGTD. With this ADE, no recursive convolution is required and the dispersive effects are equivalently represented by a time-dependent auxiliary surface polarization current governed by the ADE. For open-space problems, the hybrid DGTD and time-domain boundary integral (TDBI) algorithm [3], [4] is applied to rigorously truncate the computational domain via evaluating the field values required by incoming flux through the explicit TDBI scheme based on the equivalence principle.

This paper is organized as follows. In Section II, the theory and mathematical formulations of the DGTD-IBC algorithm are detailed. In Section III, numerical results are presented to validate the accuracy and robustness of the proposed algorithm. Conclusion is made at the end of this paper.

II. Theory and Formulation

A. Formulation of DGTD With SIBC

For a conductive object with skin depth much smaller than its thickness, the tangential components of the electric and magnetic fields over the surface of the conductor are approximately related by the SIBC [11]

$$\hat{\mathbf{n}} \times (\hat{\mathbf{n}} \times \mathbf{E}) = Z_s \cdot \hat{\mathbf{n}} \times \mathbf{H} \tag{1}$$

$$\hat{\mathbf{n}} \times (\hat{\mathbf{n}} \times \mathbf{H}) = -Y_s \cdot \hat{\mathbf{n}} \times \mathbf{E} \tag{2}$$

where $\hat{\mathbf{n}}$ is a unit normal vector pointing into the conductor, $Z_s = \sqrt{\frac{j\omega\mu}{j\omega\epsilon+\sigma}}$ is the surface impedance, and $Y_s = 1/Z_s$ is the corresponding surface admittance.

To derive the numerical flux in the presence of the SIBC [(1) and (2)], we suppose that the computational domain Ω bound by $\partial\Omega$ is split into nonoverlapping elements Ω_i with boundary $\partial\Omega_i$. According to the *Rankine–Hugoniot jump relations* along the characteristic curves for the Riemann problems, we can obtain the mathematical expression of the numerical flux for element i as [23]

$$\hat{\mathbf{n}}_{i,f} \times \mathbf{H}_f^* = \hat{\mathbf{n}}_{i,f} \times \left[\frac{\left(Z^i \mathbf{H}^i + \tilde{Z}^f \tilde{\mathbf{H}}^f \right) + \hat{\mathbf{n}}_{i,f} \times \left(\mathbf{E}^i - \tilde{\mathbf{E}}^f \right)}{Z^i + \tilde{Z}^f} \right] \tag{3}$$

$$\hat{\mathbf{n}}_{i,f} \times \mathbf{E}_f^* = \hat{\mathbf{n}}_{i,f} \times \left[\frac{\left(Y^i \mathbf{E}^i + \tilde{Y}^f \tilde{\mathbf{E}}^f \right) + \hat{\mathbf{n}}_{i,f} \times \left(\tilde{\mathbf{H}}^f - \mathbf{H}^i \right)}{Y^i + \tilde{Y}^f} \right] \tag{4}$$

where $\tilde{\mathbf{H}}^f$ and $\tilde{\mathbf{E}}^f$ are the fields from the neighboring element of element i through face f, $\hat{\mathbf{n}}_{i,f}$ is an unit outward normal vector at face f, Z^i and $\tilde{Z}^f$ are the characteristic impedance in element i and its adjacent element at face f, respectively; Y_i and $\tilde{Y}^f$ are the corresponding characteristic admittance.

Suppose that the face f_c ($f = f_c$) of element i coincides with the SIBC, (1) and (2) can be rewritten as

$$\hat{\mathbf{n}}_{f_c}^i \times (\hat{\mathbf{n}}_{f_c}^i \times \tilde{\mathbf{E}}^{f_c}) = Z_s \cdot \hat{\mathbf{n}}_{f_c}^i \times \tilde{\mathbf{H}}^{f_c} \tag{5}$$

$$\hat{\mathbf{n}}_{f_c}^i \times (\hat{\mathbf{n}}_{f_c}^i \times \tilde{\mathbf{H}}^{f_c}) = -Y_s \cdot \hat{\mathbf{n}}_{f_c}^i \times \tilde{\mathbf{E}}^{f_c}. \tag{6}$$

Substituting (5) into (3) and (6) into (4), the numerical flux flowing through the face f_c at the SIBC is simplified to

$$\hat{\mathbf{n}}_{i,f} \times \mathbf{H}_f^* = \hat{\mathbf{n}}_{i,f} \times \left[\frac{Z^i \mathbf{H}^i + \hat{\mathbf{n}}_{i,f} \times \mathbf{E}^i}{Z^i + \tilde{Z}^f} \right] \tag{7}$$

$$\hat{\mathbf{n}}_{i,f} \times \mathbf{E}_f^* = \hat{\mathbf{n}}_{i,f} \times \left[\frac{Y^i \mathbf{E}^i - \hat{\mathbf{n}}_{i,f} \times \mathbf{H}^i}{Y^i + \tilde{Y}^f} \right] \tag{8}$$

with $f = f_c$, $\tilde{Z}^{f_c} = Z_s$, and $\tilde{Y}_{f_c} = 1/Z_s$. When the conductivity $\sigma \to \infty$, the above numerical flux is simplified to $\hat{\mathbf{n}}_f^i \times \mathbf{H}_f^* = \hat{\mathbf{n}}_{i,f} \times \left(\mathbf{H}^i + \hat{\mathbf{n}}_{i,f} \times \mathbf{E}^i / Z^i \right)$ and $\hat{\mathbf{n}}_f^i \times \mathbf{E}_f^* = 0$, which is for the perfectly electric conductor (PEC) case.

However, due to the complex relation between the surface impedance Z_s and the angular frequency ω, the analytical Fourier transform is not available; thus, the time-domain counterpart of numerical flux cannot be obtained directly. To attack this problem, we first approximate the surface impedance Z_s with rational functions by the FRVF technique [28], [29] in the Laplace domain based on the Laplace transform pair $\int_0^t f(\tau) d\tau \leftrightarrow F(s)/s$.

The FRVF method approximates the samples $\{(\omega_p, Z_s(\omega_p)), \quad p = 1, \ldots, P\}$ over a frequency band by the rational functions [28], [29]

$$Z_s(s) = \sum_m^M \frac{c_m}{s-a_m} + d + se = \sum_m^M \frac{c_m s^{-1}}{1-a_m s^{-1}} + d + \frac{e}{s^{-1}} \tag{9}$$

where a_m and c_m denote the pole and the residue, respectively; a_m and c_m can either be real or come in complex conjugate pairs, d and e are two optional real parameters, M is the total number of poles. In this work, the coefficient e is set to zero. After the reduction in fractions to a common denominator and merger of similar items, we rewrite (9) as

$$Z_s(s) = \frac{u_0 + u_1 s^{-1} + u_2 s^{-2} + \cdots + u_M s^{-M}}{b_0 + b_1 s^{-1} + b_2 s^{-2} + \cdots + b_M s^{-M}} = \frac{\sum_{q=0}^M u_q s^{-q}}{\sum_{q=0}^M b_q s^{-q}}. \tag{10}$$

To solve the fitting problem in (9), the FRVF technique comprises two stages: pole identification and residue identification.

Next, the finalized Maxwell's matrix system will be derived following the standard DG process. In the Laplace domain, by applying the DG testing to the two first-order Maxwell's equations in the mesh element i, we can obtain

$$\int_{\Omega_i} \mathbf{\Phi}_k^i \cdot \left[\epsilon_i \mathbf{E}^i - s^{-1}\nabla \times \mathbf{H}^i\right] d\mathbf{r} = s^{-1} \sum_{f=1}^4 \int_{\partial\Omega_{i,f}} \mathbf{\Phi}_k^i \cdot \left[\hat{\mathbf{n}}_{i,f} \times (\mathbf{H}_f^* - \mathbf{H}^i)\right] d\mathbf{r} \tag{11}$$

$$\int_{\Omega_i} \mathbf{\Psi}_l^i \cdot \left[\mu_i \mathbf{H}^i + s^{-1}\nabla \times \mathbf{E}^i\right] d\mathbf{r} = s^{-1} \sum_{f=1}^4 \int_{\partial\Omega_{i,f}} \mathbf{\Psi}_l^i \cdot \left[\hat{\mathbf{n}}_{i,f} \times (\mathbf{E}^i - \mathbf{E}_f^*)\right] d\mathbf{r} \tag{12}$$

where i denotes the index of present mesh element, Φ_k^i and Ψ_l^i are the two testing functions for the Ampere's law and Maxwell–Faraday's law equations, respectively; $\mathbf{E}^i$ and $\mathbf{H}^i$ are the electric and magnetic fields with $\mathbf{E}^i = \sum_{k=1}^{n_e^i} e_k^i(t)\Phi_k^i(\mathbf{r})$ and $\mathbf{H}^i = \sum_{l=1}^{n_h^i} h_l^i(t)\Psi_l^i(\mathbf{r})$, n_e^i and n_h^i represent the number of corresponding basis functions in element i, f is the index of four tetrahedral faces, ϵ_i and μ_i are the permittivity and permeability in the element i, respectively.

By substituting (3) and (7) into (11), (4) and (8) into (12), we can get

$$\int_{\Omega_i} \mathbf{\Phi}_k^i \cdot \left[\epsilon_i \mathbf{E}^i - s^{-1}\nabla \times \mathbf{H}^i\right] d\mathbf{r} = s^{-1} \sum_{\substack{f=1 \\ f\neq f_c}}^4 \int_{\partial\Omega_f^i} \mathbf{\Phi}_k^i \cdot \left[\hat{\mathbf{n}}_f^i \times \frac{\tilde{Z}^f(\tilde{\mathbf{H}}^f - \mathbf{H}^i) - \hat{\mathbf{n}}_f^i \times (\tilde{\mathbf{E}}^f - \mathbf{E}^i)}{Z^i + \tilde{Z}^f}\right] d\mathbf{r} + s^{-1} \int_{\partial\Omega_{f_c}^i} \mathbf{\Phi}_k^i \cdot \left[\hat{\mathbf{n}}_{f_c}^i \times \frac{\hat{\mathbf{n}}_{f_c}^i \times \mathbf{E}^i - Z_s \mathbf{H}^i}{Z^i + Z_s}\right] d\mathbf{r} \tag{13}$$

$$\int_{\Omega_i} \mathbf{\Psi}_l^i \cdot \left[\mu_i \mathbf{H}^i + s^{-1}\nabla \times \mathbf{E}^i\right] d\mathbf{r} = s^{-1} \sum_{\substack{f=1 \\ f\neq f_c}}^4 \int_{\partial\Omega_f^i} \mathbf{\Psi}_l^i \cdot \left[\hat{\mathbf{n}}_f^i \times \frac{\tilde{Y}^f(\mathbf{E}^i - \tilde{\mathbf{E}}^f) + \hat{\mathbf{n}}_f^i \times (\mathbf{H}^i - \tilde{\mathbf{H}}^f)}{Y^i + \tilde{Y}^f}\right] d\mathbf{r} + s^{-1} \int_{\partial\Omega_{f_c}^i} \mathbf{\Psi}_l^i \cdot \left[\hat{\mathbf{n}}_{f_c}^i \times \frac{Y_s \mathbf{E}^i + \hat{\mathbf{n}}_{f_c}^i \times \mathbf{H}^i}{Y^i + Y_s}\right] d\mathbf{r}. \tag{14}$$

Substituting (10) into (13) and (14), and multiplying (13) by $Z^i + Z_s$ and (14) by $Y^i + Y_s$, then via inverse Laplace transform, we can get two semidiscretized matrix equations in integral form with respect to the time t

$$\begin{aligned}
&\bar{\mathbf{M}}_{\mathrm{ee}}^i \cdot \left[(\tilde{b}_0 + u_0)\mathbf{e}_0^i + (\tilde{b}_1 + u_1)\mathbf{e}_1^i + \cdots + (\tilde{b}_M + u_m)\mathbf{e}_M^i\right] \\
&\quad - \bar{\mathbf{S}}_{\mathrm{eh}}^i \cdot \left[(\tilde{b}_0 + u_0)\mathbf{h}_1^i + (\tilde{b}_1 + u_1)\mathbf{h}_2^i + \cdots + (\tilde{b}_M + u_M)\mathbf{h}_{M+1}^i\right] \\
&= \sum_{\substack{f=1 \\ f\neq f_c}}^4 \Big\{ \tilde{\mathbf{F}}_{\mathrm{eh}}^{i,f} \cdot \left[(\tilde{b}_0 + u_0)\tilde{\mathbf{h}}_1^f + \cdots + (\tilde{b}_M + u_M)\tilde{\mathbf{h}}_{M+1}^f\right] \\
&\quad - \bar{\mathbf{F}}_{\mathrm{eh}}^{i,f} \cdot \left[(\tilde{b}_0 + u_0)\mathbf{h}_1^i + \cdots + (\tilde{b}_M + u_M)\mathbf{h}_{M+1}^i\right] \\
&\quad - \tilde{\mathbf{F}}_{\mathrm{ee}}^{i,f} \cdot \left[(\tilde{b}_0 + u_0)\tilde{\mathbf{e}}_1^f + \cdots + (\tilde{b}_M + u_M)\tilde{\mathbf{e}}_{M+1}^f\right] \\
&\quad + \bar{\mathbf{F}}_{\mathrm{ee}}^{i,f} \cdot \left[(\tilde{b}_0 + u_0)\mathbf{e}_1^i + \cdots + (\tilde{b}_M + u_M)\mathbf{e}_{M+1}^i\right] \Big\} \\
&\quad + \bar{\mathbf{F}}_{\mathrm{ee}}^{i,f_c} \cdot \left(b_0 \mathbf{e}_1^i + \cdots + b_M \mathbf{e}_{M+1}^i\right) \\
&\quad - \bar{\mathbf{F}}_{\mathrm{eh}}^{i,f_c} \cdot \left(u_0 \mathbf{u}_1^i + \cdots + u_M \mathbf{h}_{M+1}^i\right)
\end{aligned} \tag{15}$$

$$\begin{aligned}
&\bar{\mathbf{M}}_{\mathrm{hh}}^i \cdot \left[(\tilde{u}_0 + b_0)\mathbf{h}_0^i + (\tilde{u}_1 + b_1)\mathbf{h}_1^i + \cdots + (\tilde{u}_M + b_m)\mathbf{h}_M^i\right] \\
&\quad + \bar{\mathbf{S}}_{\mathrm{he}}^i \cdot \left[(\tilde{u}_0 + b_0)\mathbf{e}_1^i + (\tilde{u}_1 + b_1)\mathbf{e}_2^i + \cdots + (\tilde{u}_M + b_M)\mathbf{e}_{M+1}^i\right] \\
&= \sum_{\substack{f=1 \\ f\neq f_c}}^4 \Big\{ \bar{\mathbf{F}}_{\mathrm{he}}^{i,f} \cdot \left[(\tilde{u}_0 + b_0)\mathbf{e}_1^i + \cdots + (\tilde{u}_M + b_M)\mathbf{e}_{M+1}^i\right] \\
&\quad - \bar{\mathbf{F}}_{\mathrm{he}}^{i,f} \cdot \left[(\tilde{u}_0 + b_0)\tilde{\mathbf{e}}_1^f + \cdots + (\tilde{u}_M + b_M)\tilde{\mathbf{e}}_{M+1}^f\right] \\
&\quad + \bar{\mathbf{F}}_{\mathrm{hh}}^{i,f} \cdot \left[(\tilde{u}_0 + b_0)\mathbf{h}_1^i + \cdots + (\tilde{u}_M + b_M)\mathbf{h}_{M+1}^i\right] \\
&\quad - \tilde{\mathbf{F}}_{\mathrm{hh}}^{i,f} \cdot \left[(\tilde{u}_0 + b_0)\tilde{\mathbf{h}}_1^f + \cdots + (\tilde{u}_M + b_M)\tilde{\mathbf{h}}_{M+1}^f\right] \Big\} \\
&\quad + \bar{\mathbf{F}}_{\mathrm{he}}^{i,f_c} \cdot \left(b_0 \mathbf{e}_1^i + \cdots + b_M \mathbf{e}_{M+1}^i\right) \\
&\quad + \bar{\mathbf{F}}_{\mathrm{hh}}^{i,f_c} \cdot \left(u_0 \mathbf{h}_1^i + \cdots + u_M \mathbf{h}_{M+1}^i\right)
\end{aligned} \tag{16}$$

where $\tilde{b}_q = Z^i b_q$, $\tilde{u}_q = Y^i u_q$, column vectors $\mathbf{e}_q^i$ and $\mathbf{h}_q^i$ comprise coefficients of basis functions $\Phi^i(r)$ for $\mathbf{E}^i$ and $\Psi^i(\mathbf{r})$ for $\mathbf{H}^i(\mathbf{r})$. The kth element of $\mathbf{e}_q^i$ and lth element of $\mathbf{h}_q^i$ is defined by

$$\{\mathbf{e}_q^i\}_k = \underbrace{\int_0^t \cdots \int_0^t}_{q} \mathrm{e}_k^i(\tau) \underbrace{d\tau \cdots d\tau}_{q} \tag{17}$$

$$\{\mathbf{h}_q^i\}_l = \underbrace{\int_0^t \cdots \int_0^t}_{q} \mathrm{h}_l^i(\tau) \underbrace{d\tau \cdots d\tau}_{q}. \tag{18}$$

The two other column vectors $\tilde{\mathbf{e}}_q^f$ and $\tilde{\mathbf{h}}_q^f$ contain the coefficients of basis functions for the fields in the neighboring

element through face f, whose elements have similar definitions as (17) and (18). The matrices $\bar{\mathbf{M}}^i_{\rm ee}$ and $\bar{\mathbf{M}}^i_{\rm hh}$ are the mass matrices, $\bar{\mathbf{S}}^i_{\rm eh}$ and $\bar{\mathbf{S}}^i_{\rm he}$ are stiffness matrices; $\bar{\mathbf{F}}^i_{\rm eh}$, $\bar{\mathbf{F}}^{i,f}_{\rm ee}$, $\bar{\mathbf{F}}^{i,f}_{\rm he}$, and $\bar{\mathbf{F}}^{i,f}_{\rm hh}$ are flux matrices for outgoing flux through face f that only requires fields in the local element i; $\tilde{\mathbf{F}}^{i,f}_{\rm ee}$, $\tilde{\mathbf{F}}^{i,f}_{\rm eh}$, $\tilde{\mathbf{F}}^{i,f}_{he}$, and $\tilde{\mathbf{F}}^{i,f}_{\rm hh}$ are flux matrices for the incoming flux via face f that only needs fields from the neighbors of element i. Their mathematical expressions are given as

$$
\begin{aligned}
\left[\bar{\mathbf{M}}^i_{\rm ee}\right]_{kl} &= \int \Phi^i_k(\mathbf{r})\cdot\epsilon^i\Phi^i_l(\mathbf{r})d\mathbf{r}\\
\left[\bar{\mathbf{M}}^i_{\rm hh}\right]_{kl} &= \int \Psi^i_k(\mathbf{r})\cdot\mu^i\Psi^i_l(\mathbf{r})d\mathbf{r}\\
\left[\bar{\mathbf{S}}^i_{\rm eh}\right]_{kl} &= \int \Phi^i_k(\mathbf{r})\cdot\nabla\times\Psi^i_l(\mathbf{r})d\mathbf{r}\\
\left[\bar{\mathbf{S}}^i_{\rm he}\right]_{kl} &= \int \Psi^i_k(\mathbf{r})\cdot\nabla\times\Phi^i_l(\mathbf{r})d\mathbf{r}\\
\left[\bar{\mathbf{F}}^{i,f}_{\rm eh}\right]_{kl} &= \frac{\tilde{Z}^f}{Z^i+\tilde{Z}^f}\int_{\partial\Omega^i_f}\Phi^i_k(\mathbf{r})\cdot\hat{\mathbf{n}}^i_f\times\Psi^i_l(\mathbf{r})d\mathbf{r}\\
\left[\tilde{\mathbf{F}}^{i,f}_{\rm eh}\right]_{kl} &= \frac{\tilde{Z}^f}{Z^i+\tilde{Z}^f}\int_{\partial\Omega^i_f}\Phi^i_k(\mathbf{r})\cdot\hat{\mathbf{n}}^i_f\times\tilde{\Psi}^{i,f}_l(\mathbf{r})d\mathbf{r}\\
\left[\bar{\mathbf{F}}^{i,f}_{\rm ee}\right]_{kl} &= \frac{1}{Z^i+\tilde{Z}^f}\int_{\partial\Omega^i_f}\Phi^i_k(\mathbf{r})\cdot\hat{\mathbf{n}}^i_f\times\hat{\mathbf{n}}^i_f\times\Phi^i_l(\mathbf{r})d\mathbf{r}\\
\left[\tilde{\mathbf{F}}^{i,f}_{\rm ee}\right]_{kl} &= \frac{1}{Z^i+\tilde{Z}^f}\int_{\partial\Omega^i_f}\Phi^i_k(\mathbf{r})\cdot\hat{\mathbf{n}}^i_f\times\hat{\mathbf{n}}^i_f\times\tilde{\Phi}^{i,f}_l(\mathbf{r})d\mathbf{r}\\
\left[\bar{\mathbf{F}}^{i,f_c}_{\rm ee}\right]_{kl} &= \int_{\partial\Omega^i_{f_c}}\Phi^i_k(\mathbf{r})\cdot\hat{\mathbf{n}}^i_{f_c}\times\hat{\mathbf{n}}^i_{f_c}\times\Phi^i_l(\mathbf{r})d\mathbf{r}\\
\left[\bar{\mathbf{F}}^{i,f_c}_{\rm eh}\right]_{kl} &= \int_{\partial\Omega^i_{f_c}}\Phi^i_k(\mathbf{r})\cdot\hat{\mathbf{n}}^i_{f_c}\times\Psi^i_l(\mathbf{r})d\mathbf{r}\\
\left[\bar{\mathbf{F}}^{i,f}_{\rm he}\right]_{kl} &= \frac{\tilde{Y}^f}{Y^i+\tilde{Y}^f}\int_{\partial\Omega^i_f}\Psi^i_k(\mathbf{r})\cdot\hat{\mathbf{n}}^i_f\times\Phi^i_l(\mathbf{r})d\mathbf{r}\\
\left[\tilde{\mathbf{F}}^{i,f}_{\rm he}\right]_{kl} &= \frac{\tilde{Y}^f}{Y^i+\tilde{Y}^f}\int_{\partial\Omega^i_f}\Psi^i_k(\mathbf{r})\cdot\hat{\mathbf{n}}^i_f\times\tilde{\Phi}^{i,f}_l(\mathbf{r})d\mathbf{r}\\
\left[\bar{\mathbf{F}}^{i,f}_{\rm hh}\right]_{kl} &= \frac{1}{Y^i+\tilde{Y}^f}\int_{\partial\Omega^i_f}\Psi^i_k(\mathbf{r})\cdot\hat{\mathbf{n}}^i_f\times\hat{\mathbf{n}}^i_f\times\Psi^i_l(\mathbf{r})d\mathbf{r}\\
\left[\tilde{\mathbf{F}}^{i,f}_{\rm hh}\right]_{kl} &= \frac{1}{Y^i+\tilde{Y}^f}\int_{\partial\Omega^i_f}\Psi^i_k(\mathbf{r})\cdot\hat{\mathbf{n}}^i_f\times\hat{\mathbf{n}}^i_f\times\tilde{\Psi}^{i,f}_l(\mathbf{r})d\mathbf{r}\\
\left[\bar{\mathbf{F}}^{i,f_c}_{\rm he}\right]_{kl} &= \int_{\partial\Omega^i_{f_c}}\Psi^i_k(\mathbf{r})\cdot\hat{\mathbf{n}}^i_{f_c}\times\Phi^i_l(\mathbf{r})d\mathbf{r}\\
\left[\bar{\mathbf{F}}^{i,f_c}_{\rm hh}\right]_{kl} &= \int_{\partial\Omega^i_{f_c}}\Psi^i_k(\mathbf{r})\cdot\hat{\mathbf{n}}^i_{f_c}\times\hat{\mathbf{n}}^i_{f_c}\times\Psi^i_l(\mathbf{r})d\mathbf{r}. \qquad (19)
\end{aligned}
$$

To obtain a fully discrete matrix equation system, the multidimensional integrations involved in (15) and (16) are approximated by the FIT using the trapezoidal integration rule, i.e., $\int_{t_1}^{t_2} f(\tau)d\tau = (t_2-t_1)[f(t_2)+f(t_1)]/2$. As a result, (17) and (18) at $t=(n+1)\delta t$ can be rewritten as

$$
\{\mathbf{e}^i_q\}_k|_{n+1} = (\delta t)^q\sum_{n_q=0}^{n}\cdots\sum_{n_2=0}^{n_3}\sum_{n_1=0}^{n_2}\left(\frac{\left[\mathrm{e}^i_k\right]_{n_1+1}+\left[\mathrm{e}^i_k\right]_{n_1}}{2}\right) \qquad (20)
$$

$$
\{\mathbf{h}^i_q\}_k|_{n+1} = (\delta t)^q\sum_{n_q=0}^{n}\cdots\sum_{n_2=0}^{n_3}\sum_{n_1=0}^{n_2}\left(\frac{\left[\mathrm{h}^i_k\right]_{n_1+1}+\left[\mathrm{h}^i_k\right]_{n_1}}{2}\right). \qquad (21)
$$

It is noted that the field values $\tilde{\mathbf{E}}^f$ and $\tilde{\mathbf{H}}^f$ in the neighboring elements used for the incoming flux evaluation are not available at $t=(n+1)\delta t$, which will result in an implicit time-marching scheme of DGTD if still employing trapezoidal integration rule. To keep the advantages of explicit DGTD, a rectangular integration rule is applied to approximate the multidimensional integration involved in $\tilde{\mathbf{E}}^f_q$ and $\tilde{\mathbf{H}}^f_q$, namely

$$
\{\tilde{\mathbf{e}}^f_q\}_k|_{n+1} = (\delta t)^q\sum_{n_q=0}^{n}\cdots\sum_{n_2=0}^{n_3}\sum_{n_1=0}^{n_2}\left[\tilde{\mathrm{e}}^f_k\right]_{n_1} \qquad (22)
$$

$$
\{\tilde{\mathbf{h}}^f_q\}_k|_{n+1} = (\delta t)^q\sum_{n_q=0}^{n}\cdots\sum_{n_2=0}^{n_3}\sum_{n_1=0}^{n_2}\left[\tilde{\mathrm{h}}^f_k\right]_{n_1}. \qquad (23)
$$

Substituting (20)–(23) into (15) and (16), and through a lengthy mathematical operation, a matrix equation is reached as

$$
\begin{pmatrix}\widehat{\mathbf{M}}^i_{\rm e} & \widehat{\mathbf{S}}^i_{\rm e}\\ \widehat{\mathbf{S}}^i_{\rm h} & \widehat{\mathbf{M}}^i_{\rm h}\end{pmatrix}\begin{bmatrix}\mathbf{e}^i_{n+1}\\ \mathbf{h}^i_{n+1}\end{bmatrix} = \begin{pmatrix}\widehat{\mathbf{F}}^i_{\rm e}\\ \widehat{\mathbf{F}}^i_{\rm h}\end{pmatrix} \qquad (24)
$$

where

$$
\begin{aligned}
\widehat{\mathbf{M}}^i_{\rm e} &= \left[(\tilde{b}_0+u_0)+\frac{\delta t}{2}(\tilde{b}_1+u_1)+\cdots+\frac{(\delta t)^M}{2}(\tilde{b}_M+u_M)\right]\bar{\mathbf{M}}^i_{\rm ee}\\
&\quad-\left[\delta t(\tilde{b}_0+u_0)+\cdots+(\delta t)^{M+1}(\tilde{b}_M+u_M)\right]\sum_{f=1,\neq f_c}^{4}\frac{\mathbf{F}^{i,f}_{\rm ee}}{2}\\
&\quad-\left[\delta t\cdot b_0+(\delta t)^2b_1+\cdots+(\delta t)^{M+1}b_M\right]\frac{\bar{\mathbf{F}}^{i,f_c}_{\rm ee}}{2} \qquad (25)\\
\widehat{\mathbf{M}}^i_{\rm h} &= \left[(\tilde{u}_0+b_0)+\frac{\delta t}{2}(\tilde{u}_1+b_1)+\cdots+\frac{(\delta t)^M}{2}(\tilde{u}_M+b_M)\right]\bar{\mathbf{M}}^i_{\rm hh}\\
&\quad-\left[\delta t(\tilde{u}_0+b_0)+\cdots+(\delta t)^{M+1}(\tilde{u}_M+b_M)\right]\sum_{f=1,\neq f_c}^{4}\frac{\mathbf{F}^{i,f}_{\rm hh}}{2}\\
&\quad-\left[\delta t\cdot u_0+(\delta t)^2u_1+\cdots+(\delta t)^{M+1}u_M\right]\frac{\bar{\mathbf{F}}^{i,f_c}_{\rm hh}}{2} \qquad (26)\\
\widehat{\mathbf{S}}^i_{\rm e} &= -\left[\delta t(\tilde{b}_0+u_0)+\cdots+(\delta t)^{M+1}(\tilde{b}_M+u_M)\right]\frac{\bar{\mathbf{S}}^i_{\rm eh}}{2}\\
&\quad+\left[\delta t(\tilde{b}_0+u_0)+\cdots+(\delta t)^{M+1}(\tilde{b}_M+u_M)\right]\sum_{f=1,\neq f_c}^{4}\frac{\bar{\mathbf{F}}^{i,f}_{\rm eh}}{2}\\
&\quad+\left[\delta t\cdot u_0+(\delta t)^2u_1+\cdots+(\delta t)^{M+1}u_M\right]\frac{\bar{\mathbf{F}}^{i,f_c}_{\rm eh}}{2} \qquad (27)\\
\widehat{\mathbf{S}}^i_{\rm h} &= \left[\delta t(\tilde{u}_0+b_0)+\cdots+(\delta t)^{M+1}(\tilde{u}_M+b_M)\right]\frac{\bar{\mathbf{S}}^i_{\rm he}}{2}\\
&\quad-\left[\delta t(\tilde{u}_0+b_0)+\cdots+(\delta t)^{M+1}(\tilde{u}_M+b_M)\right]\sum_{f=1,\neq f_c}^{4}\frac{\bar{\mathbf{F}}^{i,f}_{\rm he}}{2}\\
&\quad-\left[\delta t\cdot b_0+(\delta t)^2b_1+\cdots+(\delta t)^{M+1}b_M\right]\frac{\bar{\mathbf{F}}^{i,f_c}_{\rm he}}{2} \qquad (28)
\end{aligned}
$$

$$\begin{aligned}\widehat{\mathbf{F}}_{\mathrm{e}} =& -\mathbf{M}^i_{\mathrm{ee}}\cdot\Big[(\tilde{b}_1+u_1)\breve{\mathbf{e}}^i_1+\cdots+(\tilde{b}_M+u_M)\breve{\mathbf{e}}^i_M\Big]\\ &+\mathbf{S}^i_{\mathrm{eh}}\cdot\Big[\,(\tilde{b}_0+u_0)\breve{\mathbf{h}}^i_1+\cdots+(\tilde{b}_M+u_M)\breve{\mathbf{h}}^i_{M+1}\,\Big]\\ &+\sum_{\substack{f=1\\ f\neq f_c}}^{4}\Big\{\tilde{\mathbf{F}}^{i,f}_{\mathrm{eh}}\cdot\Big[(\tilde{b}_0+u_0)\tilde{\mathbf{h}}^f_1+\cdots+(\tilde{b}_M+u_M)\tilde{\mathbf{h}}^f_{M+1}\Big]\\ &-\bar{\mathbf{F}}^{i,f}_{\mathrm{eh}}\cdot\Big[(\tilde{b}_0+u_0)\breve{\mathbf{h}}^i_1+\cdots+(\tilde{b}_M+u_M)\breve{\mathbf{h}}^i_{M+1}\Big]\\ &-\tilde{\mathbf{F}}^{i,f}_{\mathrm{ee}}\cdot\Big[(\tilde{b}_0+u_0)\tilde{\mathbf{e}}^f_1+\cdots+(\tilde{b}_M+u_M)\tilde{\mathbf{e}}^f_{M+1}\Big]\\ &+\bar{\mathbf{F}}^{i,f}_{\mathrm{ee}}\cdot\Big[(\tilde{b}_0+u_0)\breve{\mathbf{e}}^i_1+\cdots+(\tilde{b}_M+u_M)\breve{\mathbf{e}}^i_{M+1}\Big]\Big\}\\ &+\bar{\mathbf{F}}^{i,f_c}_{\mathrm{ee}}\cdot\big(b_0\breve{\mathbf{e}}^i_1+\cdots+b_M\breve{\mathbf{e}}^i_{M+1}\big)\\ &-\bar{\mathbf{F}}^{i,f_c}_{\mathrm{eh}}\cdot\Big(u_0\breve{\mathbf{h}}^i_1+\cdots+u_M\breve{\mathbf{h}}^i_{M+1}\Big)\end{aligned}\tag{29}$$

$$\begin{aligned}\widehat{\mathbf{F}}_{\mathrm{h}} =& -\mathbf{M}^i_{\mathrm{hh}}\cdot\Big[(\tilde{u}_1+b_1)\breve{\mathbf{h}}^i_1+\cdots+(\tilde{u}_M+b_M)\breve{\mathbf{h}}^i_M\Big]\\ &-\mathbf{S}^i_{\mathrm{he}}\cdot\big[\,(\tilde{u}_0+b_0)\breve{\mathbf{e}}^i_1+\cdots+(\tilde{u}_M+b_M)\breve{\mathbf{e}}^i_{M+1}\,\big]\\ &+\sum_{\substack{f=1\\ f\neq f_c}}^{4}\Big\{\bar{\mathbf{F}}^{i,f}_{\mathrm{he}}\cdot\big[(\tilde{u}_0+b_0)\breve{\mathbf{e}}^i_1+\cdots+(\tilde{u}_M+b_M)\breve{\mathbf{e}}^i_{M+1}\big]\\ &-\tilde{\mathbf{F}}^{i,f}_{\mathrm{he}}\cdot\Big[(\tilde{u}_0+b_0)\tilde{\mathbf{e}}^f_1+\cdots+(\tilde{u}_M+b_M)\tilde{\mathbf{e}}^f_{M+1}\Big]\\ &+\bar{\mathbf{F}}^{i,f}_{\mathrm{hh}}\cdot\Big[(\tilde{u}_0+b_0)\breve{\mathbf{h}}^i_1+\cdots+(\tilde{u}_M+b_M)\breve{\mathbf{h}}^i_{M+1}\Big]\\ &-\tilde{\mathbf{F}}^{i,f}_{\mathrm{hh}}\cdot\Big[(\tilde{u}_0+b_0)\tilde{\mathbf{h}}^f_1+\cdots+(\tilde{u}_M+b_M)\tilde{\mathbf{h}}^f_{M+1}\Big]\Big\}\\ &+\bar{\mathbf{F}}^{i,f_c}_{\mathrm{he}}\cdot\big(b_0\breve{\mathbf{e}}^i_1+\cdots+b_M\breve{\mathbf{e}}^i_{M+1}\big)\\ &+\bar{\mathbf{F}}^{i,f_c}_{\mathrm{hh}}\cdot\Big(u_0\breve{\mathbf{h}}^i_1+\cdots+u_M\breve{\mathbf{h}}^i_{M+1}\Big)\end{aligned}\tag{30}$$

with

$$\breve{\mathbf{e}}^i_q|_{n+1}=\mathbf{e}^i_q|_{n+1}-(\delta t)^q\mathbf{e}^i_{n+1}/2\tag{31}$$

$$\breve{\mathbf{h}}^i_q|_{n+1}=\mathbf{h}^i_q|_{n+1}-(\delta t)^q\mathbf{h}^i_{n+1}/2\tag{32}$$

$$\breve{\mathbf{e}}^i_0|_{n+1}=0\tag{33}$$

$$\breve{\mathbf{h}}^i_0|_{n+1}=0.\tag{34}$$

In order to efficiently address the multidimensional sum when evaluating $\tilde{\mathbf{e}}^f_q$ (22), $\tilde{\mathbf{h}}^f_q$ (23), $\breve{\mathbf{e}}^i_q$ (31), and $\breve{\mathbf{h}}^i_q$ (32), four recursive formulae are introduced

$$\tilde{\mathbf{e}}^f_q|_{n+1}=\tilde{\mathbf{e}}^f_q|_n+\delta t\cdot\tilde{\mathbf{e}}^f_{q-1}|_{n+1}\tag{35}$$

$$\tilde{\mathbf{h}}^f_q|_{n+1}=\tilde{\mathbf{h}}^f_q|_n+\delta t\cdot\tilde{\mathbf{h}}^f_{q-1}|_{n+1}\tag{36}$$

$$\breve{\mathbf{e}}^i_q|_{n+1}=\breve{\mathbf{e}}^i_q|_n+\delta t\cdot\breve{\mathbf{e}}^i_{q-1}|_{n+1}+(\delta t)^q\cdot\frac{\mathbf{e}^i_n}{2}\tag{37}$$

$$\breve{\mathbf{h}}^i_q|_{n+1}=\breve{\mathbf{h}}^i_q|_n+\delta t\cdot\breve{\mathbf{h}}^i_{q-1}|_{n+1}+(\delta t)^q\cdot\frac{\mathbf{h}^i_n}{2}.\tag{38}$$

The dimension of the locally coupled matrix equation in (24) is $(n^i_e+n^i_h)\times(n^i_e+n^i_h)$. In DGTD analysis, the inversion of the coupling matrix is precalculated and stored before launching the time-marching scheme. Thus, the computational cost with FIT is on the order of $(n^i_e+n^i_h)\times(n^i_e+n^i_h)\times\mathcal{O}(N')$ with N' denoting the total number of elements over the ∂_{SIBC}. For elements not touching the ∂_{SIBC}, the fourth-order Runge–Kutta (RK) method is exploited. The corresponding computational is on the order of $(n^i_e\times n^i_e+n^i_h\times n^i_h)\times\mathcal{O}(N'')$ with N'' representing the total number of elements not over the ∂_{SIBC}.

B. Formulation of DGTD With TIBC for Graphene

The above SIBC-enhanced DGTD solver is only valid for conducting objects with skin depth much smaller than the thickness; it fails for thin conductive sheet with much larger attenuation length for instance a graphene sheet. To handle this situation, a TIBC-augmented DGTD scheme is detailed in this part to characterize the electromagnetic properties of graphene from microwave to THz bands. As 2-D material with atoms arranged into a honeycomb lattice having thickness around 0.34 nm, graphene has significant potential applications in transistors [31], surface plasmon waveguides [33], THz antennas [32], etc. The intrinsic properties of graphene can be dynamically manipulated by tunning its surface conductivity $\sigma_g(\omega,\mu_c,\Gamma,T)$ which is the function of angular frequency ω, chemical potential μ_c, scattering rate Γ, and temperature T. For a nonmagnetized graphene in the THz band, according to the kubo formula [34], the expression of surface conductivity is given by

$$\sigma_g=-\frac{j\sigma_0}{(\omega-j2\Gamma)}\tag{39}$$

with

$$\sigma_0=\frac{q^2k_BT}{\pi\hbar^2}\left[\frac{\mu_c}{k_BT}+2\ln\Big(e^{-\mu_c/k_BT}+1\Big)\right].\tag{40}$$

To model the graphene, instead of straightforwardly volumetric meshing, a TIBC given by [19], [20]

$$\hat{\mathbf{n}}\times(\mathbf{H}^+-\mathbf{H}^-)=\sigma_g\mathbf{E}_t\tag{41}$$

can be used to replace the graphene, where the superscripts $+$ and $-$ denote the upper and lower faces of graphene, respectively; $\hat{\mathbf{n}}$ is a unit normal vector pointing from lower to upper face.

One way to incorporate this TIBC into DGTD is using the same method as above based on the fact that the surface conductivity in the Laplace domain can be written as

$$\sigma_g=\frac{\sigma_0}{s+2\Gamma}=\frac{s^{-1}\sigma_0}{1+2\Gamma s^{-1}}\tag{42}$$

which can be regarded as a rational function with only one pole $a_1=-2\Gamma$ and residue $c_1=\sigma_0$. Via the inverse Laplace transform, the time-domain matrix equations will be obtained.

Instead of using the FIT method, an ADE method is applied by introducing an auxiliary surface polarization current $\mathbf{J}$

$$\mathbf{J}(\omega)=\sigma_g\mathbf{E}_t(\omega).\tag{43}$$

Based on the ADE method, the multidimensional integral operation in the temporal space is avoided and the dispersive effect is replaced by a time-dependent auxiliary surface current. The time-domain counterpart of (43) can be written as

$$\frac{\partial\mathbf{J}}{\partial t}+2\Gamma\cdot\mathbf{J}=\sigma_0\mathbf{E}_t.\tag{44}$$

Based upon the *Rankine–Hugoniot jump relations*, the numerical flux subject to the TIBC in (41) is revised as

$$\hat{\mathbf{n}}_{i,f}\times\mathbf{H}_f^* = \hat{\mathbf{n}}_{i,f}\times\left[\frac{\left(Z^i\mathbf{H}^i+\tilde{Z}^f\tilde{\mathbf{H}}^f\right)+\hat{\mathbf{n}}_{i,f}\times\left(\mathbf{E}^i-\tilde{\mathbf{E}}^f\right)}{Z^i+\tilde{Z}^f}+\alpha_g\frac{\tilde{Z}^f\mathbf{J}^i_{f_g}}{\left(Z^i+\tilde{Z}^f\right)}\right] \tag{45}$$

$$\hat{\mathbf{n}}_{i,f}\times\mathbf{E}_f^* = \hat{\mathbf{n}}_{i,f}\times\left[\frac{\left(Y^i\mathbf{E}^i+\tilde{Y}^f\tilde{\mathbf{E}}^f\right)+\hat{\mathbf{n}}_{i,f}\times\left(\tilde{\mathbf{H}}^f-\mathbf{H}^i\right)}{Y^i+\tilde{Y}^f}-\alpha_g\frac{\mathbf{J}^i_{f_g}}{2\left(Y^i+\tilde{Y}^f\right)}\right] \tag{46}$$

where f_g denote the face index of element i overlapping the TIBC, $\alpha_g=1$ if $f=f_g$ otherwise $\alpha_g=0$.

To construct the DGTD matrix system, the auxiliary surface current $\mathbf{J}$ is approximated by $\boldsymbol{\varphi}^i(\mathbf{r})=\hat{\mathbf{n}}_{i,f_g}\times\Phi^i(\mathbf{r})\times\hat{\mathbf{n}}_{i,f_g}$

$$\mathbf{J}^i=\sum_{p=1}^{n_g^i}c_p^i(t)\boldsymbol{\varphi}_p^i(\mathbf{r}) \tag{47}$$

with c_p^i denoting time-dependent expansion coefficient, n_g^i representing the number of basis functions. In this work, $n_g^i=6$ since six edge basis functions not over the face f_g have no tangential components according to the properties of edge vector basis functions [2].

To facilitate DGTD operation, the DG testing is applied to the two first-order time-derivative Maxwell's curl equations and the ADE in (44); the time-domain matrix equations can be obtained as

$$\bar{\mathbf{M}}^i_{ee}\frac{\partial\mathbf{e}^i}{\partial t}=\bar{\mathbf{S}}^i_{eh}\mathbf{h}^i+\sum_{f=1}^{4}\left(\bar{\mathbf{F}}^{i,f}_{ee}\mathbf{e}^i+\tilde{\bar{\mathbf{F}}}^{i,f}_{ee}\tilde{\mathbf{e}}_f+\bar{\mathbf{F}}^{i,f}_{eh}\mathbf{h}^i+\tilde{\bar{\mathbf{F}}}^{i,f}_{eh}\tilde{\mathbf{h}}^f\right)+\alpha_g\bar{\mathbf{F}}_{eg}\mathbf{c}^i \tag{48}$$

$$\bar{\mathbf{M}}^i_{hh}\frac{\partial\mathbf{h}^i}{\partial t}=-\bar{\mathbf{S}}^i_{he}\mathbf{e}^i+\sum_{f=1}^{4}\left(\bar{\mathbf{F}}^{i,f}_{hh}\mathbf{h}^i+\tilde{\bar{\mathbf{F}}}^{i,f}_{hh}\tilde{\mathbf{h}}^f+\bar{\mathbf{F}}^{if}_{he}\mathbf{e}^i+\tilde{\bar{\mathbf{F}}}^{i,f}_{he}\tilde{\mathbf{e}}^f\right)+\alpha_g\bar{\mathbf{F}}_{hg}\mathbf{c}^i \tag{49}$$

$$\bar{\mathbf{J}}^i\frac{\partial\mathbf{c}^i}{\partial t}=-2\Gamma\bar{\mathbf{J}}^i\mathbf{c}^i+\sigma_0\bar{\mathbf{M}}^i_c\mathbf{e}^i \tag{50}$$

where

$$\left[\bar{\mathbf{J}}^i\right]_{kl}=\int_{\partial\Omega^i_{f_g}}\boldsymbol{\varphi}^i_k(\mathbf{r})\cdot\boldsymbol{\varphi}^i_l(\mathbf{r})d\mathbf{r} \tag{51}$$

$$\left[\bar{\mathbf{M}}_c\right]_{kl}=\int_{\partial\Omega^i_{f_g}}\boldsymbol{\varphi}^i_k(\mathbf{r})\cdot\Phi^i_l(\mathbf{r})d\mathbf{r} \tag{52}$$

$$\left[\bar{\mathbf{F}}^{ii,f_g}_{ec}\right]_{kl}=\frac{\tilde{Z}^i_f}{Z^i+\tilde{Z}^f}\int_{\partial\Omega^i_{f_g}}\boldsymbol{\Phi}^i(\mathbf{r})\cdot\boldsymbol{\varphi}^i_l(\mathbf{r})d\mathbf{r} \tag{53}$$

$$\left[\bar{\mathbf{F}}^{ii,f_g}_{he}\right]_{kl}=\frac{1}{Y^i+\tilde{Y}^f}\int_{\partial\Omega^i_{f_g}}\boldsymbol{\Psi}^i_k(\mathbf{r})\cdot(\hat{\mathbf{n}}_{i,f_g}\times\boldsymbol{\varphi}^i_l(\mathbf{r}))d\mathbf{r}. \tag{54}$$

The semidiscrete matrix equations (48)–(50) will be solved by the standard RK method.

Since (24) and (48)–(50) have been solved with an explicit time-marching scheme the CFL-like condition must be satisfied to ensure stability. In this work, the time step size δt is determined in terms of the following condition [4], [30]:

$$c_0\delta t\le\min\{l_{\min}\sqrt{\epsilon_r\mu_r}/4(p+1)^2\} \tag{55}$$

where c_0 is the free-space light speed, p is the order of basis function, and $l_{\min}$ is the minimum edge length.

C. Hybrid DGTD and TDBI Scheme [4]

For differential equation solvers, the computational domain of DGTD has to be exactly and efficiently truncated for open-region problems. At the truncation boundary $\partial\Omega$, the field values $\tilde{\mathbf{E}}^f$ and $\tilde{\mathbf{H}}^f$ used for the incoming flux (the total numerical flux can be split into two parts: outgoing and incoming flux. The outgoing flux only requires the field values in present element, while the incoming flux needs the field values from its neighbors) calculation in (3), (7), (45), and (46) are evaluated by the time-domain boundary integral (TDBI) algorithm on the basis of Huygens' principle [35], [36] with equivalent electric and magnetic currents explicitly calculated from the DGTD scheme [4]. This method is mathematically exact and only involves forward matrix–vector product operation. The truncation boundary can be conformal to the surface of the scattering object, and more importantly locally truncated boundary can be applied to the disconnected scatterers. Thereby, the resulting computational domain can be as small as possible.

III. Numerical Results

To validate and demonstrate the accuracy of this proposed algorithm, the scattering from various conductive structures are investigated. For the excitation, a sinusoidally modulated Gaussian plane wave defined as $\mathbf{E}^{\text{inc}}(\mathbf{r},t)=\hat{\mathbf{p}}E_0G(t-\hat{\mathbf{k}}\cdot\mathbf{r}/c_0)$, where $\hat{\mathbf{p}}=\hat{\mathbf{x}}$ is the polarization, $\hat{\mathbf{k}}=\hat{\mathbf{z}}$ is the direction of propagation, $E_0=1$ V/m is the amplitude, and $G(t)=\exp(-[t-t_0]^2/\tau_m^2)\cos(2\pi f_m[t-t_0])$ is a Gaussian pulse with modulation frequency f_m, delay t_0, and duration τ_m.

A. Spherical Scattering Cluster

For the first example, a scatterer comprising of three disconnected spheres [4] with conductivity $\sigma=5.8$ as shown in Fig. 1 is studied. The surface impedance Z_s is approximated by rational functions with five poles as listed in Table I. The fitted value and the original data are shown in Fig. 2, which shows very good consistency. The parameters of the excitation are set as: $\tau_m=2/(\pi\times10^9)$ s, $t_0=5\tau_m$, and $f_m=10^9$ Hz. As shown in Fig. 1, each sphere is locally truncated by the its own conformal boundary, thus resulting in smaller number of unknowns. Based on the Huygens' principle, the fields required for incoming flux evaluation at the truncation boundary are calculated by the TDBI according to the equivalent currents over the Huygens' surface (dashed yellow curve). In this example,

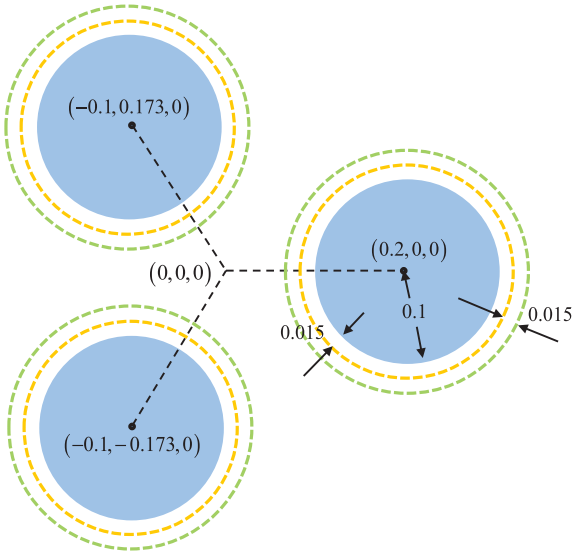

Fig. 1. Scattering cluster comprises three imperfectly conducting spheres [4]. All dimensions are in meters.

TABLE I
POLES a_m AND RESIDUES c_m FOR THE SURFACE IMPEDANCE Z_s WITH $\sigma = 5.8$ M/S, AND THE OPTIONAL PARAMETER $d = 306.3762$

m	a_m	c_m
1	-2.3071×10^{11}	-5.1707×10^{13}
2	-0.4059×10^{11}	-0.1517×10^{13}
3	-0.1424×10^{11}	-0.0247×10^{13}
4	-0.0524×10^{11}	-0.0061×10^{13}
5	-0.0133×10^{11}	-0.0014×10^{13}

the total number of tetrahedrons is 29 647, and the time step sizes for DGTD and TDBI are 1.39×10^{-12} and 2.13×10^{-11} s, respectively. In Fig. 3, the calculated RCS at 1.0003 GHz is provided. For comparison, the reference by the finite-element-boundary-integral (FE-BI) algorithm is also presented. Very good agreements are noted.

B. Magnetized Plasma and Dielectric-Coated Sphere

In the second example, a conductive sphere coated by different dielectric layer is investigated. For convenience, it is supposed that this sphere has same conductivity as the above spherical cluster but with radius $R = 0.3$ m. Besides, a same Gaussian pulse is utilized as the transient excitation. First, We assume that there is only one dielectric layer with thickness $h_1 = 0.015$ m and relative permittivity $\epsilon_r = 1.5$ covers this sphere. For this example, 97 067 tetrahedrons are involved, and the time step sizes for DGTD and TDBI are 1.3899×10^{-12} and 2.6875×10^{-11} s. In Fig. 4, the RCS calculated by the SIBC enhanced DGTD-BI algorithm is presented. Also, the reference obtained by FE-BI method is provided for comparison. Very good agreements are observed as well.

Next, we assume that this dielectric-coated sphere is covered by an additional magnetized plasma layer with thickness

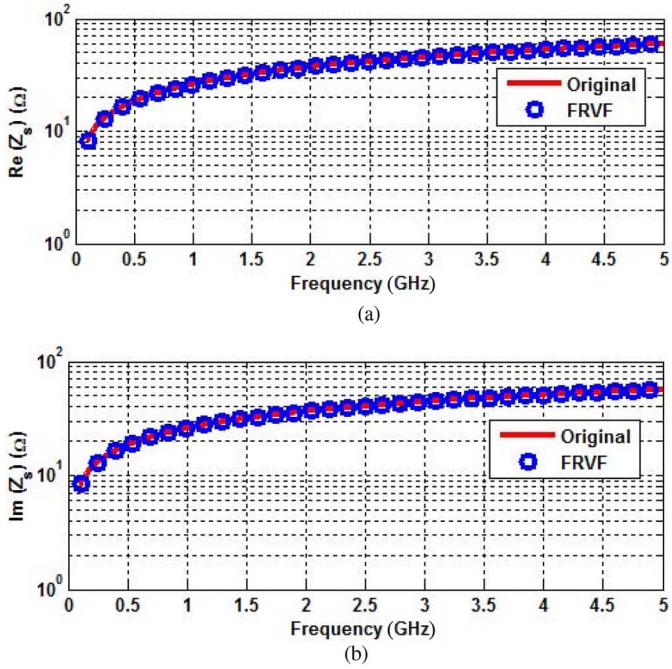

Fig. 2. Approximated surface impedance Z_s from 100 MHz to 5 GHz using FRVF method with five poles.

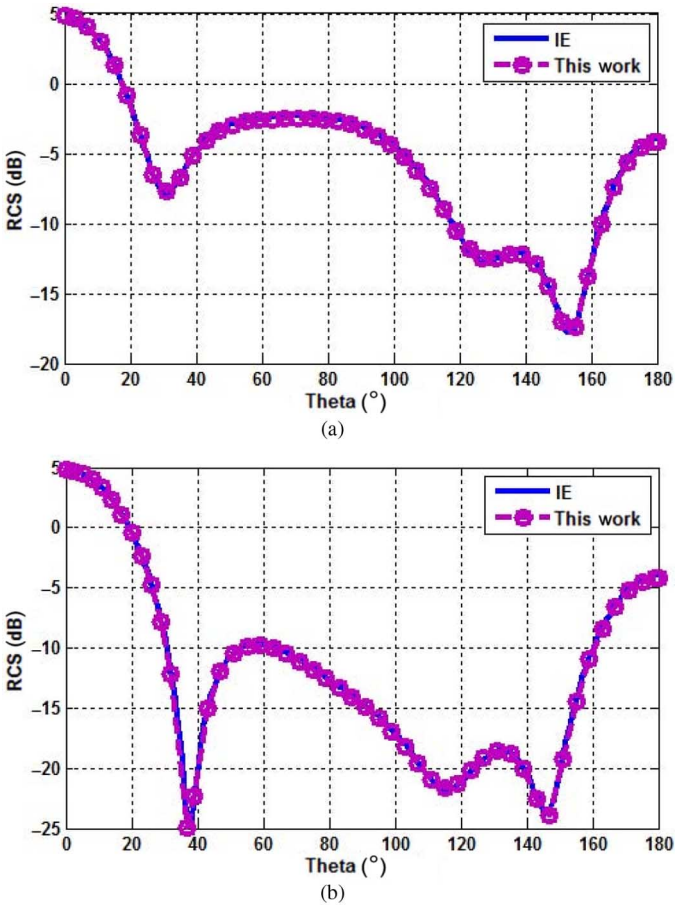

Fig. 3. RCS on (a) xz- and (b) yz-planes computed at 1.002 GHz from the DGTD-SIBC algorithm and IE method.

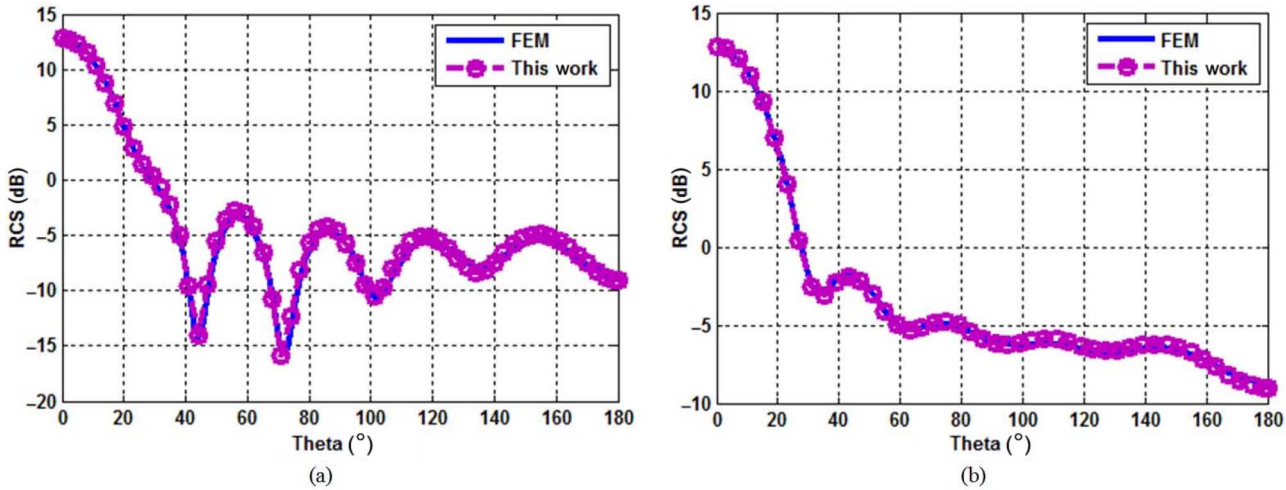

Fig. 4. RCS on (a) xz- and (b) yz-planes computed at 1.002 GHz from the DGTD-SIBC algorithm and FE-BI approach.

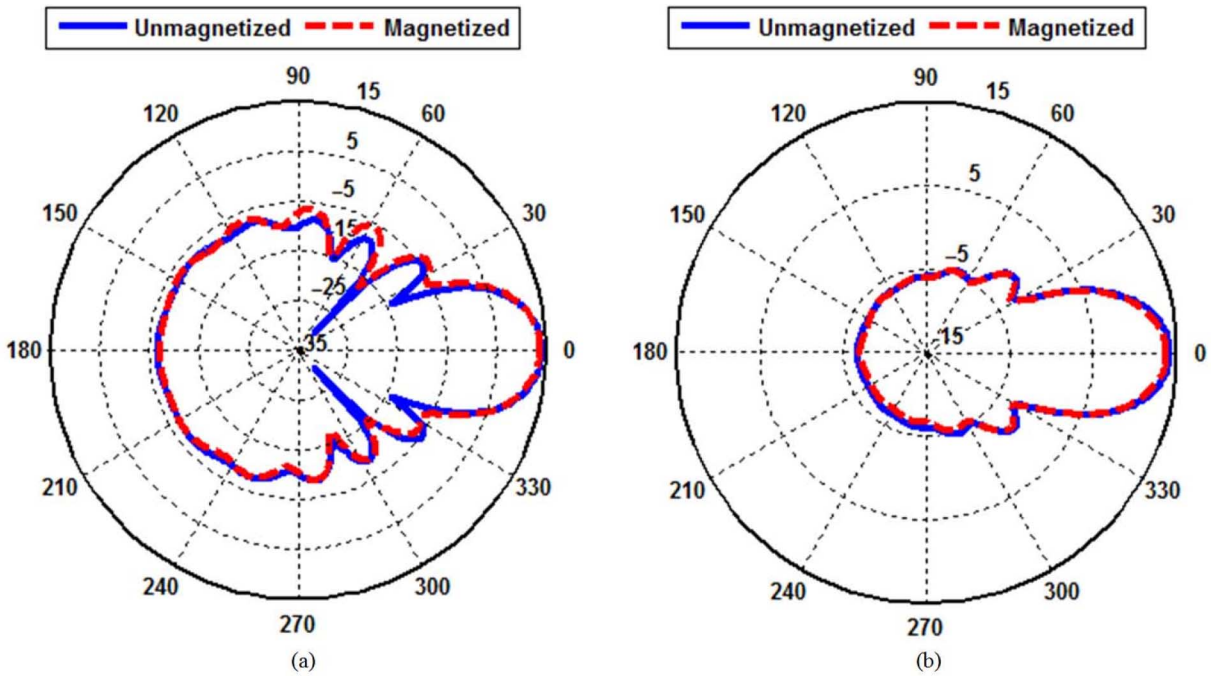

Fig. 5. Computed RCS of the plasma-coated sphere on (a) xz- and (b) yz-planes computed at 1.003 GHz.

$h_2 = 0.015$ m apart from the above dielectric layer. For the magnetized plasma, the permittivity becomes a frequency-dependent tensor $\bar{\bar{\epsilon}}$ [37]. For instance, the permittivity for the plasma with a z-directed magnetostatic field $\mathbf{B}_0 = B_0\hat{\mathbf{z}}$ is given by [37]

$$\bar{\bar{\epsilon}}_z = \begin{pmatrix} \epsilon_{xx} & j\epsilon_{xy} & 0 \\ -j\epsilon_{yx} & \epsilon_{yy} & 0 \\ 0 & 0 & \epsilon_{zz} \end{pmatrix}^z \tag{56}$$

with

$$\epsilon_{zz} = \epsilon_0 \left[1 - \frac{\omega_p^2}{\omega(\omega - j\upsilon_e)}\right]$$

$$\epsilon_{xx}^z = \epsilon_{yy}^z = \epsilon_0 \left[1 - \frac{(\omega_p/\omega)^2[1 - (j\upsilon_e/\omega)]}{[1 - (j\upsilon_e/\omega)]^2 - (\omega_{C_e}^z/\omega)^2}\right]$$

$$\epsilon_{xy}^z = \epsilon_{yx}^z = -\epsilon_0 \frac{(\omega_p/\omega)^2(\omega_{C_e}^z/\omega)}{[1 - (j\upsilon_e/\omega))]^2 - (\omega_{C_e}^z/\omega)^2}$$

where ω_p, υ_e, and $\omega_{C_e}^z$ denote the plasma frequency (for an arbitrarily static magnetic bias, $\boldsymbol{\omega}_{C_e} = \omega_{C_e}^x\hat{\mathbf{x}} + \omega_{C_e}^y\hat{\mathbf{y}} + \omega_{C_e}^z\hat{\mathbf{z}}$), electron collision rate, and cyclotron frequency, respectively. To model the magnetized plasma by DGTD, an ADE method is employed by introducing an auxiliary volume polarization current density $\mathbf{P}(\mathbf{r}, t)$ into the Maxwell–Faraday's law equation. The ADE governing the current density $\mathbf{P}$ is defined as [37]

$$\partial_t\mathbf{P} + \upsilon_e\mathbf{P} = \epsilon_0\omega_p^2\mathbf{E} + \boldsymbol{\omega}_{C_e} \times \mathbf{P}. \tag{57}$$

To study the effects of the plasma layer, we first calculate the RCS for the unmagnetized case with $\omega_p = \pi \times 2.8 \times 10^9$ Hz and $\upsilon_e = 2\pi \times 10^9$. Then, the RCS for magnetized plasma with $\omega_{C_e}^x = \omega_{C_e}^y = \omega_{C_e}^z = 2\pi \times 10^9$ Hz is computed. In Fig. 5,

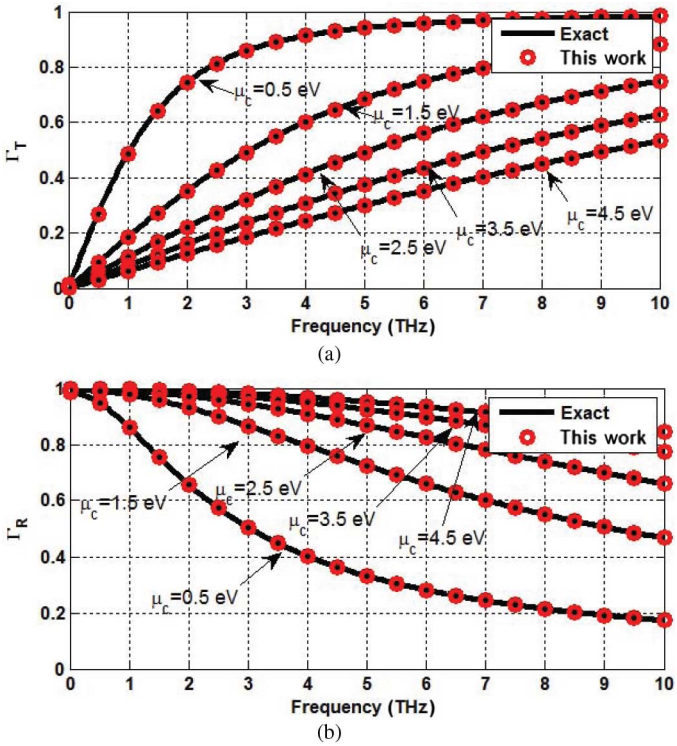

Fig. 6. Calculated (a) insertion loss (or transmission) $\Gamma_{\rm T}$ and (b) reflection coefficient $\Gamma_{\rm R}$ versus different chemical potential μ_c but with fixed scattering rate $\Gamma = 0.35\,\text{meV}/2\pi\hbar$.

the detailed RCS plots are shown. As can be seen, for the unmagnetized plasma, the RCS is symmetric. In the presence of static magnetic field, the RCS becomes antisymmetric due to the presence of Lorentz force which causes Faraday rotation.

C. Parallel-Plate Waveguide Loaded by a Graphene Sheet

In this example, the propagating properties of a plane wave in a z-directed parallel-plate waveguide intercepted by a graphene sheet are studied. The backward and forward plates are perfectly electric conductor (PEC), and the left and right plates are perfectly magnetic conductor (PMC). The two ends of the waveguide are truncated by Silver–Müller absorption boundary condition (SM-ABC). The parameters of the Gaussian pulse are set as: $f_m = 5 \times 10^{12}$ Hz, $\tau_m = 2/(\pi \times 10^{13})$ s, and $t_0 = 10\tau_m$. By launching the plane wave at the near-end of the waveguide, the insertion loss ΓT and reflection ΓR can be obtained for different chemical potentials, as shown in Fig. 6. To verify the accuracy of the proposed algorithm, the exact solution given by $\Gamma_T = 1 + \Gamma_R$ and $\Gamma_R = -\frac{\sigma_g \eta_0}{2+\sigma_g \eta_0}$ [19], [38] are also presented, where η_0 denotes the characteristic impedances in free space. As expected, excellent agreements are achieved. It is interestingly noted that the transmission degrades but the reflection becomes significant as the increasing of the chemical potential, which is attributed that the conductivity of the graphene becomes larger (more like an effective conductor) as μ_c increases.

D. 5 by 10 μm^2-Graphene Patch

To validate the proposed DGTB-TIBC algorithm for graphene modeling, a $5 \times 10\,\mu\text{m}^2$-graphene patch in [39] under the illumination of a normally incident plane wave with modulation frequency $f_m = 2.5$ THz, duration $\tau_m = 1.274 \times 10^{-13}$ s, and delay $t_0 = 3t_m$ is revisited. The parameters of the surface conductivity σ_g are given by $T = 300$ K, $\mu_c = 0$ eV, and $\Gamma = \frac{1}{2\tau}$ with $\tau = 10^{-13}$ s. The figure-of-merits for this example are either the total scattering-cross-section (TSCS), the absorption-cross-section (ACS), the extinction-cross-section (ECS), or the surface plasmon resonances (SPR). In this example, the normalized ECS from 0.1 to 4 THz are calculated by the proposed DGTD-RBC algorithm, as shown in Fig. 7. For comparison, the numerical result in [39] obtained by IE method is also shown. Apparently, good agreements are observed.

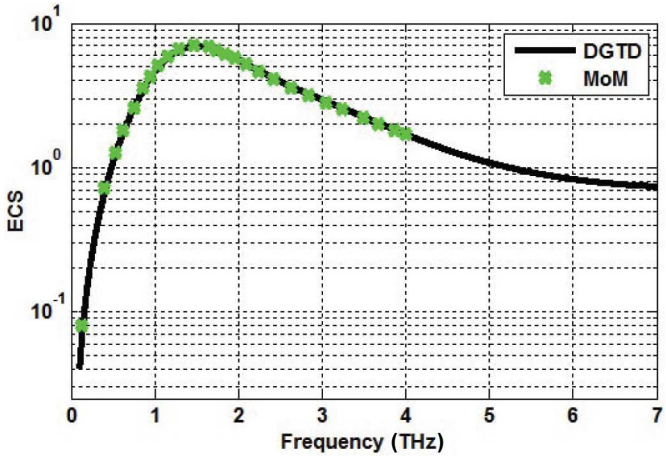

Fig. 7. Comparison of the normalized ECS and the reference result calculated by DGTD-TIBC and the IE method [39].

E. Nonmagnetized Micrometer Graphene Ribbon

In the last example, a graphene ribbon with width $w = 20\,\mu\text{m}$ and length $l = 100\,\mu\text{m}$ in the xy-plane is characterized by the proposed DGTD-TIBC algorithm. The time step sizes for DGTD and TDBI of this example are 1.1068×10^{-16} and 2.6919×10^{-15}, respectively; the total number of tetrahedrons involved in this example is 102 758. For this example, we set $f_m = 5 \times 10^{12}$ Hz, $\tau_m = 2/\pi \times 10^{13}$ s, $t_0 = 3\tau_m$, $T = 300$ K, and $\Gamma = 0.25\,\text{meV}/2\pi\hbar$.

First, the TSCS versus different chemical potentials μ_c is investigated, as shown in Fig. 8. To obtain the TSCS, we use the formula given as

$$\text{TSCS} = \frac{\oint_S \mathbf{E}_s \times \mathbf{H}_s^* dS}{||\mathbf{E}_{\text{inc}} \times \mathbf{H}_{\text{inc}}^*||} \tag{58}$$

where $\mathbf{E}_s$ and $\mathbf{H}_s$ denote the scattered fields, the superscript $*$ represents complex conjugate, $\mathbf{E}_{\text{inc}}$ and $\mathbf{H}_{\text{inc}}$ are the incident fields, and S is a surface enclosing the graphene. It is first noted from Fig. 8 that the TSCS displays sharp maxima at some frequency points in the THz band, which are due to the far-field enhancement resulted from the surface plasmon resonances. Also, the surface plasmon resonant frequencies are up-shifted with higher μ_c. The reason behind this phenomenon is that higher chemical potential requires more photon energy

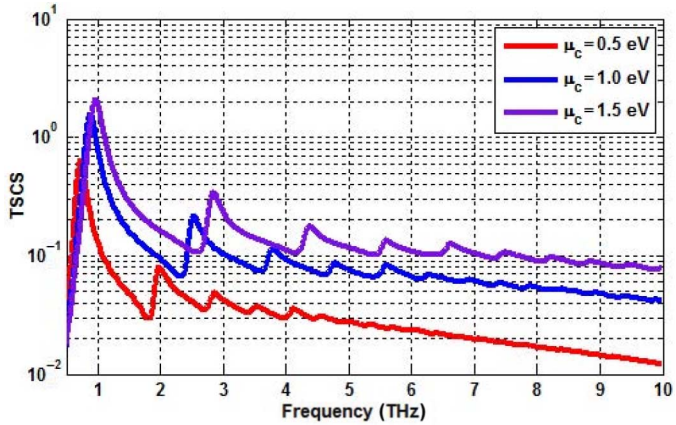

Fig. 8. Normalized total cross-scattering-section (TSCS) corresponds to different chemical potentials.

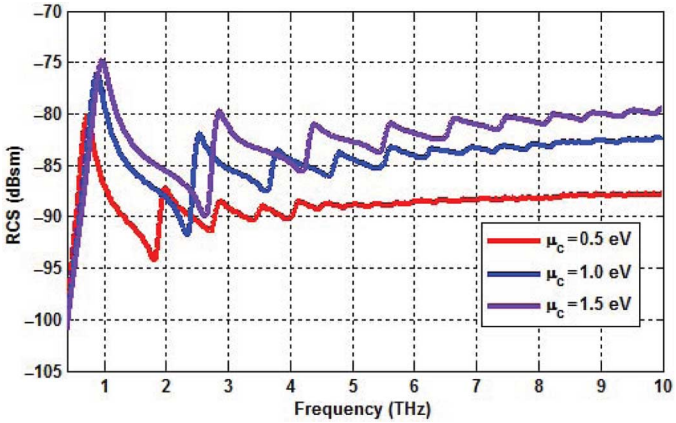

Fig. 9. Calculated forward bistatic RCS of the graphene ribbon corresponding to different chemical potentials

to excite the resonance, where the photon energy E is proportional to frequency, namely $E = \hbar\omega$. Also, the forward bistatic RCSs corresponding to different chemical potentials are presented in Fig. 9. It is observed that the peaks of the RCS happen at the same frequency as the TSCS and higher chemical potential results in stronger scattering. To verify the strongly local field confinement, the distributions of the electric field E_x at the first two resonant frequencies $f_1 = 0.9541$ and $f_2 = 2.806$ THz for $\mu_c = 1.5$ eV case are plotted in Fig. 10. To have a basic insight into the far-field pattern, the normalized far-field radiations in the E-plane at the above two frequencies are shown in Fig. 11. It is interestingly noted that the far-field patterns at $f_1 = 0.9541$ and $f_2 = 2.806$ THz are very similar to a half-wavelength dipole and one and a half-wavelength dipole, respectively. This is attributed that the current distribution $\mathbf{J} = \sigma_g \mathbf{E}_t$ is very similar to the dipole's current as shown in Fig. 10.

Next, to show the effects of oblique incident wave (propagating in the yz-plane) on the plasmon resonance, the propagating wave vector $\hat{\mathbf{k}}$ is redefined as $\hat{\mathbf{k}} = \sin(\theta)\hat{\mathbf{y}} + \cos(\theta)\hat{\mathbf{z}}$ with θ denoting the angle between the wave vector $\hat{\mathbf{k}}$ and z-axis. The calculated TSCSs corresponding to different incident angles for the E-polarized wave (vector $\mathbf{H}$ calculated by $\hat{\mathbf{k}} \times \mathbf{E}/\eta_0$ is across the graphene ribbon) are presented in Fig. 12. It is noted

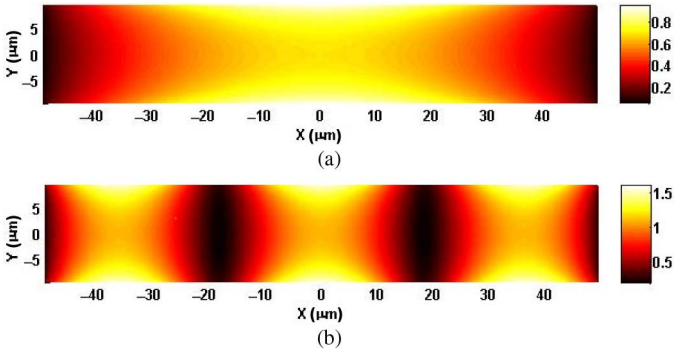

Fig. 10. Magnitude distribution of the normalized electric field E_x over the graphene sheet at resonant frequencies $f_1 = 0.9541$ THz (a) and $f_2 = 2.806$ THz (b). Based on the current distribution, the periodicity at f_1 is around one third of that at f_2, which complies with the frequency ratio $f_2/f_1 \approx 3$.

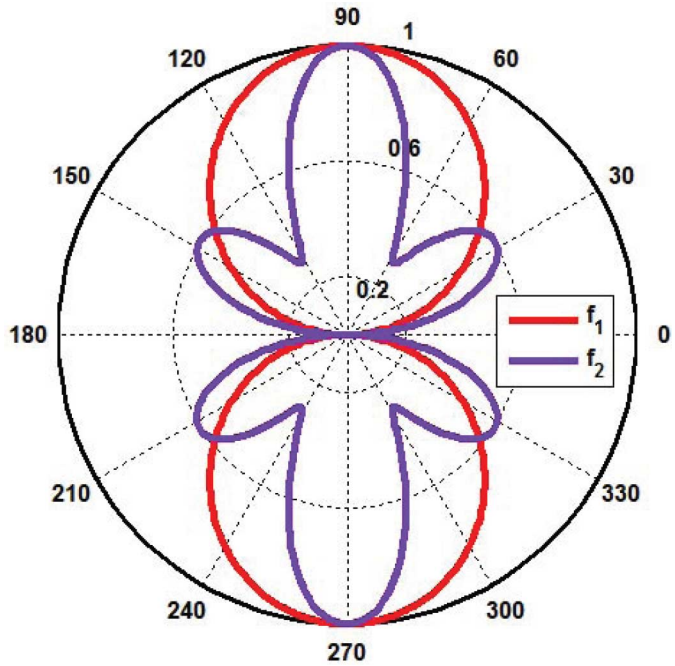

Fig. 11. Normalized far-field patterns at $f_1 = 0.9541$ THz and $f_2 = 2.806$ THz for $\mu_c = 1.5$ eV case.

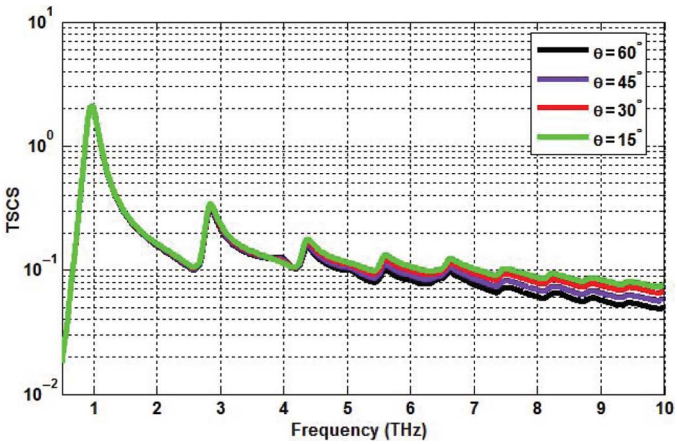

Fig. 12. Normalized total cross-scattering-section (TSCS) versus different incident angles for E-polarized wave.

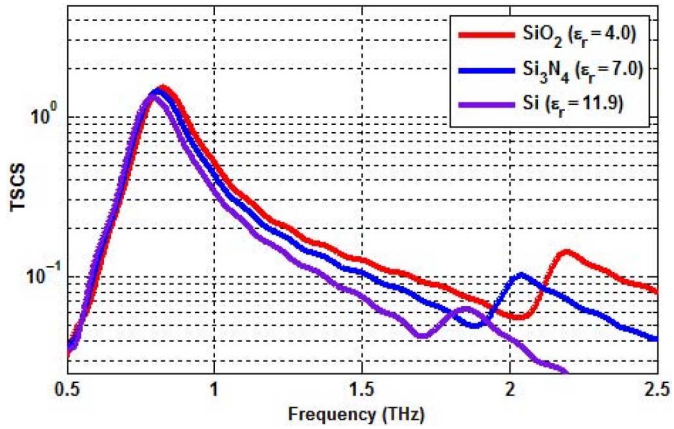

Fig. 13. Normalized total cross-scattering-section (TSCS) versus different dielectric substrates.

that the magnitudes of resonant peaks at higher order plasmon modes are pronouncedly influenced.

Finally, to have a better understanding about the impacts of substrates on the SPR, we assume that the graphene ribbon is covered by two dielectric slabs with 2 μm thickness. In Fig. 13, the TSCS versus substrates with different permittivities are presented. We observe that the resonant frequencies are shifted down to the low-frequency region for higher permittivity substrate. This is due to the fact that the physical dimension of the graphene becomes larger compared with wavelength $\lambda = \lambda_0/\sqrt{\epsilon_r}$.

IV. Conclusion

In this paper, the DGTD algorithm combined with the SIBC is developed to analyze the scattering from finite conducting objects with skin depth much smaller than the conductor's thickness. Then, the DGTD is further integrated with the TIBC to study the electromagnetic properties of graphene in the THz band. Due to the application of IBC, the volumetric discretization is avoided, which results in reduced number of unknowns and improved CFL number for the explicit time-marching scheme. Various numerical examples are provided to verify the accuracy and feasibility of the proposed algorithm.

Acknowledgment

The authors would like to thank the reviewers for their insightful comments and valuable suggestions that significantly improve the quality of this work.

References

[1] A. Taflove and S. C. Hagness, *Computational Electrodynamics: The Finite-Difference Time-Domain Method*, 3rd ed. Norwood, MA, USA: Artech House, 2005.

[2] J. M. Jin, *The Finite Element Method in Electromagnetics*, 2nd ed. Hoboken, NJ, USA: Wiley, 2003.

[3] P. Li, Y. Shi, L. J. Jiang, and H. Bağcı, "A discontinuous Galerkin time domain-boundary integral method for analyzing transient electromagnetic scattering," in *Proc. IEEE Int. Symp. Antennas Propag.*, Jul. 6–11, 2014, pp. 1893–1894.

[4] P. Li, Y. Shi, L. J. Jiang, and H. Bagci, "A hybrid time-domain discontinuous Galerkin-boundary integral method for electromagnetic scattering analysis," *IEEE Trans. Antennas Propag.*, vol. 62, no. 5, pp. 2841–2846, May 2014.

[5] A. Karlsson, "Approximate boundary conditions for thin structures," *IEEE Trans. Antennas Propag.*, vol. 57, no. 7, pp. 144–148, Jan. 2009.

[6] J. H. Beggs, R. J. Luebbers, K. S. Yee, and K. S. Kunz, "Finite-difference time-domain implementation of surface impedance boundary conditions," *IEEE Trans. Antennas Propag.*, vol. 40, no. 1, pp. 49–56, Jan. 1992.

[7] G. Kobidze, "Implementation of collocated surface impedance boundary conditions in FDTD," *IEEE Trans. Antennas Propag.*, vol. 58, no. 7, pp. 2394–2403, Jul. 2010.

[8] M. Yi, M. Ha, Z. Qian, A. Aydiner, and M. Swaminthan, "Skin-effect-incorporated transient simulation using the Laguerre-FDTD scheme," *IEEE Trans. Microw. Theory Techn.*, vol. 61, no. 12, pp. 4029–4039, Dec. 2013.

[9] S. Yan and J. M. Jin, "Self-dual integral equations for electromagnetic scattering from IBC objects," *IEEE Trans. Antennas Propag.*, vol. 61, no. 11, pp. 5533–5545, Nov. 2013.

[10] N. Ida, L. D. Rienzo, and S. Yuferev, "Surface impedance boundary conditions-application to computer-aided electromagnetic design," presented at 11th Int. Conf. Develop. Appl. Syst., Suceava, Romania, May 17–19, 2012.

[11] M. A. Leontovich, "On the approximate boundary conditions for electromagnetic fields on the surface of well conducting bodies," *in Investigations of Propagation of Radio Waves*, B. A. Vvedensky, Ed. Moscow, Russia: Academy of Sciences USSR, 1948, pp. 5–20.

[12] T. B. A. Senior, "Impedance boundary conditions for imperfectly conducting surfaces," *Appl. Sci. Res. B*, vol. 8, pp. 418–436, 1960.

[13] R. V. Sabariego, P. Dular, C. Geuzaine, and J. Gyselinck, "Surface-impedance boundary conditions in dual time-domain finite-element formulation," *IEEE Trans. Magn.*, vol. 46, no. 8, pp. 3524–3531, Aug. 2010.

[14] J. Gyselinck, P. Dular, C. Geuzaine, and R. V. Sabariego, "Surface-impedance boundary conditions in time-domain finite-element calculations using the magnetic-vector-potential formulation," *IEEE Trans. Magn.*, vol. 45, no. 3, pp. 1280–1283, Mar. 2009.

[15] A. W. Glisson, "Electromagnetic scattering by arbitrarily shaped surfaces with impedance boundary conditions," *Radio Sci.*, vol. 27, no. 6, pp. 935–943, 1992.

[16] P. Y.-Oijala, S. P. Kiminki, and S. Jarvenpaa, "Solving IBC-CFIE with dual basis functions," *IEEE Trans. Antennas Propag.*, vol. 58, no. 12, pp. 3997–4004, Dec. 2010.

[17] M. Feliziani, "Subcell FDTD modeling of field penetration through lossy shields," *IEEE Trans. Electromagn. Compat.*, vol. 54, no. 2, pp. 299–307, Apr. 2012.

[18] V. Nayyeri, M. Soleimani, and O. M. Ramahi, "A method to model thin conductive layers in the finite-difference time-domain method," *IEEE Trans. Electromagn. Compat.*, vol. 56, no. 2, pp. 385–392, Apr. 2014.

[19] G. Hanson, "Dyadic Green's functions and guided waves for a surface conductivity model of graphene," *J. Appl. Phys.*, vol. 103, no. 064302, Mar. 2008.

[20] V. Nayyeri, M. Soleimani, and M. Ramahi, "Wideband modeling of graphene using the finite-difference time-domain metod," *IEEE Trans. Antennas Propag.*, vol. 6, no. 12, pp. 6107–6114, Dec. 2013.

[21] O. V. Shapoval, J. S. Gomez-Diaz, J. Perruisseau-Carrier, J. R. Mosig, and A. I. Nosich, "Integral equation analysis of plane wave scattering by coplanar graphene-strip gratings in the THz range," *IEEE Trans. Terahertz Sci. Technol.*, vol. 6, no. 3, pp. 666–674, Sep. 2013.

[22] K. Q. Costa, V. Dmitriev, C. M. Nascimento, and G. L. Silvano, "Theoretical analysis of graphene nanoantennas with different shapes," *Microw. Opt. Lett.*, vol. 56, no. 5, pp. 1019–1024, May 2014.

[23] K. Sankaran, "Accurate domian truncation techniques for time-domain conformal methods," Ph.D. dissertation, Dept. Inf. Technol. Elect. Eng., ETH Zurich, Zurich, Switzerland, 2007.

[24] J. S. Hesthaven and T. Warburton, *Nodal Discontinuous Galerkin Methods*. New York, NY, USA: Springer, 2008.

[25] P. Li and L. J. Jiang, "A hybrid electromagnetics-circuit simulation method exploiting discontinuous Galerkin finite element time domain method," *IEEE Microw. Wireless Compon. Lett.*, vol. 23, no. 3, pp. 113–115, Mar. 2013.

[26] P. Li, L. J. Jiang, and H. Bagci, "Co-simulation of electromagnetics circuit systems exploiting DGTD and MNA," *IEEE Trans. Compon. Packag. Manuf. Technol.*, vol. 4, no. 6, pp. 1052–1061, Jun. 2014.

[27] P. Li and L. J. Jiang, "Integration of arbitrary lumped multiport circuit networks into the discontinuous Galerkin time-domain analysis," *IEEE Trans. Microw. Theory Techn.*, vol. 61, no. 7, pp. 2525–2534, Jul. 2013.

[28] B. Gustavsen and A. Semlyen, "Rational approximation of frequency domian responses by vector fitting," *IEEE Trans. Power Del.*, vol. 14, no. 3, pp. 1052–1061, Jul. 1999.
[29] B. Gustavsen, "Improving the pole relocating properties of vector fitting," *IEEE Trans. Power Del.*, vol. 21, no. 3, pp. 1587–1592, Jul. 2006.
[30] S. D. Gedney, J. C. Yong, T. C. Kramer, and J. A. Roden, "A discontinuous Galerkin finite element time-domain method modeling of dispersive media," *IEEE Trans. Antennas Propag.*, vol. 60, no. 4, pp. 1969–1977, Apr. 2012.
[31] F. schwierz, "Graphene transistors," *Nat. Nanotechnol.*, vol. 5, pp. 487–496, Jul. 2010.
[32] M. Tamagnone, J. S. Gomez-Diaz, J. R. Mosig, and J. P. Carrier, "Analysis and design of terahertz antennas based on plasmonic resonant graphene sheets," *Appl. Phys. Lett.*, vol. 101, no. 214102, pp. 1–4, 2012.
[33] M. Jablan, M. Soljacic, and H. Buljan, "Plasmons in graphene: Fundamental properties and potential applications," *Proc. IEEE*, vol. 101, no. 7, pp. 1689–1704, Jul. 2013.
[34] R. Kubo, "Statistical-mechanical theory of irreversible processes. I. General theory and simple applications to magnetic and conduction problems," *J. Phys. Soc. Jpn.*, vol. 12, no. 6, pp. 570–586, 1957.
[35] P. Li and L. J. Jiang, "The far field transformation for the antenna modeling based on spherical electric field measurements," *Prog. Electromagn. Res. Lett.*, vol. 123, pp. 243–261, 2012.
[36] P. Li, Y. Li, L. J. Jiang, and J. Hu, "A wide-band equivalent source reconstruction method exploiting the Stoer-Bulirsch algorithm with the adaptive frequency sampling," *IEEE Trans. Antennas Propag.*, vol. 61, no. 10, pp. 5338–5343, Oct. 2013.
[37] P. Li and L. J. Jiang, "Simulation of electromagnetic waves in the magnetized cold plasma by a DGFETD method," *IEEE Antennas Wireless Propag. Lett.*, vol. 12, pp. 1244–1247, Dec. 2013.
[38] G. Lovat, "Equivalent circuit for electromagnetic interaction and transmission through graphene sheets," *IEEE Trans. Electromagn. Compat.*, vol. 54, no. 1, pp. 101–109, Feb. 2012.
[39] I. Llsater, C. Kremers, A. Cabellos-Aparicio, J. M. Jornet, E. Alarcon, and D. N. Chigrin, "Graphene-based nano-patch antenna for terahertz radiation," *Photonics Nanostruct.: Fundam. Appl.*, vol. 10, pp. 353–358, May 2012.

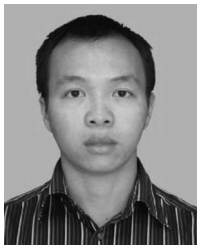

Ping Li (S'12–M'15) is currently pursuing the Ph.D. degree at the Center of Electromagnetics and Optics, University of Hong Kong, Pokfulam Road, Hong Kong.

His research interests include the near-field to far-field transformation techniques, phaseless equivalent source reconstruction methods, discontinuous Galerkin time-domain method, and uncertainty quantification for large scale electromagnetic systems. Dr. Li has been serving as the Reviewers for several international journals, including the IEEE TRANSACTIONS ON MICROWAVE THEORY AND TECHNIQUES, the IEEE TRANSACTIONS ON ANTENNAS AND PROPAGATION, the IEEE ANTENNAS AND WIRELESS PROPAGATION LETTERS, the PROCEEDINGS OF IEEE, *Journal of Electromagnetic Waves and Applications*, and *ACES Journal*. He has authored more than 10 journal papers in the IEEE TRANSACTIONS ON MICROWAVE THEORY AND TECHNIQUES, the IEEE TRANSACTIONS ON ANTENNAS AND PROPAGATION, the IEEE TRANSACTIONS ON ELECTROMAGNETIC CAPABILITY, the IEEE TRANSACTIONS ON COMPONENTS, PACKAGING, AND MANUFACTURING TECHNOLOGY, etc. His papers were selected as the Finalist papers in the 29th International Review of Progress in Applied Computational Electromagnetics and the 2014 IEEE International Symposium on Electromagnetic Compatibility. In 12th International Workshop on Finite Elements for Microwave Engineering, he was awarded the Student Paper Award.

Yifei Shi (S'09–M'12) was born in Jiangsu, China, in 1981. He received the B.E. degree in electronic and information engineering from Nanjing Tech University, Nanjing, Jiangsu, China, in 2004, and the Ph.D. degree in electromagnetic field and microwave technology from Nanjing University of Science and Technology, Nanjing, Jiangsu, China, in 2012.

Since 2012, he has been a Postdoctoral Research Fellow with the Department of Electrical Engineering, King Abdullah University of Science and Technology, Thuwal, Saudi Arabia. His research interest includes time-domain IE.

Li Jun Jiang (S'01–M'04–SM'13) received the B.S. degree in electrical engineering from Beijing University of Aeronautics and Astronautics, Beijing, China, in 1993, the M.S. degree in electronic engineering from Tsinghua University, Beijing, China, in 1996, and the Ph.D. degree in electrical and computer engineering from the University of Illinois at Urbana-Champaign, Champaign, IL, USA, in 2004.

From 1996 to 1999, he was an Application Engineer with the Hewlett-Packard Company. Since 2004, he has been the Postdoctoral Researcher, the Research Staff Member, and the Senior Engineer with IBM T.J. Watson Research Center. Since the end of 2009, he has been an Associate Professor with the Department of Electrical and Electronic Engineering, University of Hong Kong, Pok Fu Lam, Hong Kong.

Dr. Jiang is the Associate Editor of the IEEE TRANSACTIONS ON ANTENNAS AND PROPAGATION, the Associate Editor of *Progress in Electromagnetics Research*, the Associate Guest Editor of the PROCEEDINGS OF IEEE Special Issue in 2011–2012, an ACES Member, and a Member of Chinese Computational Electromagnetics Society. He was the Semiconductor Research Cooperation (SRC) Industrial Liaison for several academic projects. He has been served as the Scientific Consultant with Hong Kong Applied Science and Technology Research Institute Company Limited (Hong Kong ASTRI) from 2010 to 2011, the Panelist of the Expert Review Panel (ERP) of Hong Kong R&D Centre for Logistics and Supply Chain Management Enabling Technologies since 2013. Since June 2013, he has also been the Senior Visiting Professor at Tsinghua University. He was the TPC Chair of the 7th International Conference on Nanophotonics (ICNP)/the 3rd Conference on Advances in Optoelectronics and Micro/Nano Optics (AOM), the TPC Co-Chair of the 12th International Workshop on Finite Elements for Microwave Engineering, the Co-Chair of the 2013 International Workshop on Pulsed Electromagnetic Field with Delft, the Netherlands, the General Chair of the 2014 IEEE 14th HK AP/MTT Postgraduate Conference. He has been the Elected TPC Member of the IEEE EPEP since 2014, the TPC Member of the IEEE EDAPS since 2010, the TPC Member of the 2013 IEEE ICMTCE, the Scientific Committee Member of the 2010 IEEE SMEE, the special session organizers of IEEE EDAPS, IEEE EMC, ACES, AP-RASC, PIERS, Co-Organizer of HKU Computational Science and Engineering Workshops from 2010 to 2012, the TC-9 and TC-10 Member of the IEEE EMC-S since 2011, and session Chairs of many international conferences. He also served as the Reviewer of IEEE transactions on several topics, and other primary electromagnetics and microwave-related journals. He was the recipient of the IEEE MTT Graduate Fellowship Award in 2003 and the Y.T. Lo Outstanding Research Award in 2004.

Hakan Bağcı (S'98–M'07–SM'14) received the B.S. degree in electrical and electronics engineering from Bilkent University, Ankara, Turkey, in 2001, and the M.S. and Ph.D. degrees in electrical and computer engineering from the University of Illinois at Urbana-Champaign (UIUC), Champaign, IL, USA, in 2003 and 2007, respectively.

From June 1999 to July 2001, he worked as an Undergraduate Researcher with the Computational Electromagnetics Group, Bilkent University. From August 2001 to December 2006, he was a Research Assistant with the Center for Computational Electromagnetics and Electromagnetics Laboratory, UIUC. From January 2007 to August 2009, he worked as a Research Fellow with the Radiation Laboratory, University of Michigan, Ann Arbor, MI, USA. In August 2009, he joined the Division of Physical Sciences and Engineering, King Abdullah University of Science and Technology (KAUST) as Assistant Professor of Electrical Engineering. He authored and coauthored eight finalist papers in the student paper competitions at the 2005, 2008, and 2010 IEEE Antennas and Propagation Society International Symposiums and 2013 and 2014 Applied Computational Electromagnetics Society Conference. His research interests include various aspects of computational electromagnetics with emphasis on time-domain IEs and their fast marching-on-in-time-based solutions, well-conditioned integral-equation formulations, and development of fast hybrid methods for analyzing statistical EMC/EMI phenomena on complex and fully loaded platforms.

Dr. Bağcı was the recipient of the 2008 International Union of Radio Scientists (URSI) Young Scientist Award and the 2004–2005 Interdisciplinary Graduate Fellowship from the Department of Computational Science and Engineering, UIUC. His paper titled *Fast and Rigorous Analysis of EMC/EMI Phenomena on Electrically Large and Complex Structures Loaded With Coaxial Cables* was one of the three finalists (with honorable mention) for the 2008 Richard B. Schulz Best Transactions Paper Award given by the IEEE Electromagnetic Compatibility Society.